Chinese Chemical Letters 33 (2022) 1468–1474

Contents lists available at ScienceDirect

Chinese Chemical Letters

journal homepage: www.elsevier.com/locate/cclet

Ingeniously designed Ni-Mo-S/$ZnIn_2S_4$ composite for multi-photocatalytic reaction systems

Jing Chen[a], Yumei Tang[a], Shihao Wang[a], Lingbin Xie[b], Cheng Chang[a], Xiaolei Cheng[a], Mingming Liu[a], Longlu Wang[a,*], Lianhui Wang[b]

[a] College of Electronic and Optical Engineering & College of Microelectronics, Jiangsu Province Engineering Research Center for Fabrication and Application of Special Optical Fiber Materials and Devices, Nanjing University of Posts and Telecommunications, Nanjing 210023, China
[b] State Key Laboratory of Organic Electronics and Information Displays & Jiangsu Key Laboratory for Biosensors, Institute of Advanced Materials (IAM) & Institute of Flexible Electronics (Future Technology), Nanjing University of Posts and Telecommunications, Nanjing 210023, China

ARTICLE INFO

Article history:
Received 24 July 2021
Revised 19 August 2021
Accepted 23 August 2021
Available online 27 August 2021

Keywords:
Molybdenum disulfide (MoS_2)
Ni-Mo-S nanosheets
Multi-reaction systems
Hydrogen evolution reaction (HER)
Atomic doping strategy

ABSTRACT

Molybdenum disulfide (MoS_2) with low cost, high activity and high earth abundance has been found to be a promising catalyst for the hydrogen evolution reaction (HER), but its catalytic activity is considerably limited due to its inert basal planes. Here, through the combination of theory and experiment, we propose that doping Ni in MoS_2 as catalyst can make it have excellent catalytic activity in different reaction systems. In the EY/TEOA system, the maximum hydrogen production rate of EY/Ni-Mo-S is 2.72 times higher than that of pure EY, which confirms the strong hydrogen evolution activity of Ni-Mo-S nanosheets as catalysts. In the lactic acid and Na_2S/Na_2SO_3 systems, when Ni-Mo-S is used as co-catalyst to compound with $ZnIn_2S_4$ (termed as Ni-Mo-S/$ZnIn_2S_4$), the maximum hydrogen evolution rates in the two systems are 5.28 and 2.33 times higher than those of pure $ZnIn_2S_4$, respectively. The difference in HER enhancement is because different systems lead to different sources of protons, thus affecting hydrogen evolution activity. Theoretically, we further demonstrate that the Ni-Mo-S nanosheets have a narrower band gap than MoS_2, which is conducive to the rapid transfer of charge carriers and thus result in multi-photocatalytic reaction systems with excellent activity. The proposed atomic doping strategy provides a simple and promising approach for the design of photocatalysts with high activity and stability in multi-reaction systems.

Nowadays, with the rapid development of industrialization and the rapid growth of people's demand, traditional fossil fuels are increasingly exhausted [1–4]. Society is facing the dual pressure of environmental pollution and energy shortage. Therefore, there is an urgent need for mankind to actively explore and develop new energy sources while making effective use of fossil fuels in order to gradually replace the existing fossil energy sources [5–7]. As an important energy carrier, molecular hydrogen as an ideal green energy is characterized by high energy density and high safety. Photocatalysis technology provides a feasible tactic to produce hydrogen energy since Fujishima and Honda demonstrated photoelectrochemical reaction to prepare hydrogen from water splitting by using TiO_2 photoelectrode in 1972. The key of catalytic hydrogen production lies in the development and utilization of catalytic materials [8–11].

For photocatalytic catalysts, electrons and protons produced in sunlight are mainly used to reduce hydrogen ions to produce hydrogen [12–14]. For a catalyst with excellent performance, it is indispensable for hydrogen production to have a catalyst that can absorb visible light and generate a large number of charge carriers and a co-catalyst with abundant active centers [15]. Among many photocatalysts, $ZnIn_2S_4$ has become one of the most promising materials for visible light hydrogen evolution due to its narrow band gap and good chemical stability, which has attracted extensive attention of researchers [16–19]. However, the high rate of photoexcited charge recombination and narrow light absorption range make $ZnIn_2S_4$ unable to utilize solar energy effectively, which limits its photocatalytic efficiency [20]. As a co-catalyst, MoS_2 has attracted much attention due to its low cost, high activity and high abundance, which can be comparable to Pt in improving the efficiency of photocatalytic hydrogen evolution to the greatest extent [21–26]. Now a large number of studies have proved that MoS_2, as an excellent photocatalytic material, is mainly suitable for hydrogen production under acidic conditions, but has poor performance

* Corresponding author.
E-mail address: wanglonglu@hnu.edu.cn (L. Wang).

https://doi.org/10.1016/j.cclet.2021.08.103
1001-8417/

under alkaline conditions [27–32]. More recently, Jian Zhang *et al.* have reported that Ni-MoS_2 nanosheets with chemical composition of $Ni_{0.13}Mo_{0.87}S_2$ were prepared by hydrothermal reaction, which proved that nickel doping can enhance the electrocatalytic hydrogen evolution of MoS_2 under alkaline conditions [33]. Although much efforts have been made to improve the hydrogen evolution efficiency of photocatalysts in acidic or alkaline conditions, there is a lack of studies on the development of photocatalytic material suitable for multi-reaction systems, which have good performance in both acidic and alkaline conditions or even neutral conditions [34–42]. Therefore, it is of great significance to develop a photocatalyst with multi-reaction systems for practical application.

In this paper, we report a simple hydrothermal strategy for the synthesis of Ni-Mo-S nanosheets. The HER activity of Ni doped with MoS_2 substrate in multi-reaction systems was systematically studied. It is found that the introduction of nickel ions (Ni^{2+}) in the precursor solution and the medium environment play an important role in regulating the intrinsic properties of MoS_2. Our theoretical calculations show that the monatomic Ni dopant occupies the Mo site in MoS_2 to expose the high density unsaturated sulfur site, leading to significant electronic structure changes on the MoS_2 catalytic inert base plane to promote water dissociation and subsequent catalytic processes. This is the reason for the enhancement of HER catalytic activity of MoS_2 in acidic, neutral and alkaline solutions. The results show that the combination of Ni-Mo-S nanosheets and appropriate semiconductor $ZnIn_2S_4$ is a reasonable strategy for the construction of an efficient photocatalytic system.

In this work, zinc acetate dihydrate ($Zn(CH_3COO)_2{\cdot}2H_2O$), indium chloride tetrahydrate ($InCl_3{\cdot}4H_2O$), thiourea (CH_4N_2S), ammonium molybdatetetrahydrate ($(NH_4)_6Mo_7O_{24}{\cdot}4H_2O$), nickel sulfate hexahydrate ($NiSO_4{\cdot}6H_2O$), triethanolamine (TEOA), lactic acid, sodium sulfide nonahydrate($Na_2S{\cdot}9H_2O$), sodium sulfite (Na_2SO_3)were purchased from Sinopherm Chemical Reagents Co., Ltd. (Shanghai, China). All reagents and materials can be used without additional purification. The deionized water used in the experiment was from local sources.

$ZnIn_2S_4$ was synthesized by solvothermal method. First, 0.08 g of $Zn(CH_3COO)_2{\cdot}2H_2O$, 0.15 g of CH_4N_2S and 0.10 g of $InCl_3{\cdot}4H_2O$ are weighed in a 100 mL beaker, and then 16 mL of ethylenediamine and water (the concentration is 1:1) mixed solution is added to the beaker and stirred for 30 min. After the solid is completely dissolved, the reaction mixture is transferred into a 25 mL Teflon-lined stainless steel autoclaveand sealed. The stainless steel autoclave with Teflon liner was heated at 160 °C for 12 h and then cooled to room temperature. The black turbidity liquid was centrifuged, washed with ethanol and centrifuged several times, and then placed in a vacuum drying oven to dry at 60 °C for 8 h.

Ni-Mo-S was synthesized by hydrothermal method. $(NH_4)_6Mo_7O_{24}{\cdot}4H_2O$, $NiSO_4{\cdot}6H_2O$ and CH_4N_2S were used as molybdenum, nickel and sulfur sources, respectively. In order to study the influence of different proportions of Ni and Mo precursors on hydrogen evolution performance, the ratio of Ni and Mo was changed by changing the amount of added nickel source. 0.71 g $(NH_4)_6Mo_7O_{24}{\cdot}4H_2O$, 0.53 g $NiSO_4{\cdot}6H_2O$ and 3.21 g CH_4N_2S (the Ni and Mo precursor ratio is 1:2) were dispersed in 80 mL deionized water by rapid stirring to prepare mixed aqueous solution. The solution was then transferred to a 100 mL stainless steel autoclave lined with Teflon. After 24 h of heating at 200 °C, it was naturally cooled to room temperature and repeatedly washed with deionized water to remove impurities and unreacted precursors. Finally, the obtained material was dried in a vacuum oven at 50 °C for 48 h.

The 20 mg $ZnIn_2S_4$ and 2 mg Ni-Mo-S powders synthesized by the above method were uniformly mixed by mortar grinding to prepare $ZnIn_2S_4$/Ni-Mo-S composite materials.

The morphology of the catalyst was observed by Hitachi S-4800 scanning electron microscope (SEM), and the microstructure of the catalyst was studied by TECNAI G2 F30 S-TWIN transmission electron microscope (TEM). High-resolution TEM (HRTEM) photomicrographs were obtained with an energy dispersive X-ray spectrometer (EDX) at 200 kV. X-ray photoelectron spectroscopy (XPS) analysis was performed on a Thermo Escalab 250XI spectrometer using a monochromatic Al Kσ source (1486.6 eV). The spectral binding energy was C 1s binding energy at 284.6 eV for reference. The XPS data was analyzed using Casa XPS software. Ultraviolet-visible diffuse reflection (UV-vis DRS) absorption spectra were obtained on a Hitachi UV-4100 spectrometer, using $BaSO_4$ as the reference standard. Photoluminescence (PL) spectra were measured using an F-4700 FL type fluorescence spectrophotometer with an excitation wavelength of 400 nm.

In this study, the band structure and the density of states of Ni-Mo-S are realized by the ultrasoft pseudopotential method of plane waves based on density functional theory (DFT). The Cambridge Sequence Total Energy Package (CASTEP) code was used for geometric optimization, and the exchange correlation interaction was processed by the Perdew-Burke-Ernzerhof of the generalized gradient approximation (GGA-PBE). In the process of geometric optimization, the total energy was 2.0×10^{-5} eV/atom, the maximum force was 0.05 eV/Å, the maximum displacement was 0.02 Å, and the maximum stress was 0.1 GPa. Convergence tests are required before geometric optimization. According to the convergence test, the tolerance of self-consistent field (SCF) is 5.0×10^{-6} eV/atom, and the plane wave energy cutoff (E_{cut}) is determined to be 350 eV. The Brillouin region with $3 \times 3 \times 2$ K-grid was sampled by Monkhorst−Pack for electron convergence test.

Photocatalytic hydrogen evolution experiments were carried out in a sealed quartz flask of 100 mL at room temperature and atmospheric pressure. A 300 W xenon lamp (PLS-SXE300, Beijing Xendetong Technology Co., Ltd., China) was used as the light source, and equipped with a cut-off filter (Kenko L-42) to remove the ultraviolet light with a wavelength less than 420 nm, and the photocatalytic reaction was carried out at 10 cm away from the light source. In an acidic or alkaline reaction system, the prepared 20 mg $ZnIn_2S_4$ photocatalyst powder and 2.35 mg Ni-Mo-S co-catalyst powder were weighed. The prepared photocatalyst was dispersed in 100 mL mixed aqueous solution containing 15 mL lactic acid (pH 2.5) or 0.35 mol/L $Na_2S{\cdot}9H_2O$ and 0.25 mol/L Na_2SO_3 (pH 13.2) as sacrifice reagents. In the neutral reaction system, 20 mg of Eosin Y (EY) dye sensitizer and 20 mg of Ni-Mo-S photocatalyst powder were dispersed in 100.0 mL of mixed aqueous solution containing 15 mL of triethanolamine (pH 7) as sacrifice reagent. The mixed aqueous solution was ultrasonic treated for 10 min and transferred to 100 mL sealed quartz bottle reactor for hydrogen evolution. Before the photocatalytic reaction, the system was degassed by bubbling argon for 20 min to ensure that the reaction took place in an inert environment. During the photocatalytic reaction, the temperature of the reaction system was kept at 25 °C by circulating water pump and irradiation source. In order to eliminate the precipitation of the mixed solution and ensure the uniformity, the magnetic stirring (400 r/min) was maintained throughout the photocatalytic hydrogen production test. Gas chromatography with A built-in thermal conductivity detector (TCD) and a 5 Å molecular sieve column was used for online analysis of hydrogen production, with nitrogen as the carrier gas.

The schematic diagram of the preparation process of $ZnIn_2S_4$ and Ni-Mo-S is shown in Fig. 1a. The micromorphology of $ZnIn_2S_4$ and Ni-Mo-S samples with different Ni loads were observed by scanning electron microscopy (SEM). Fig. 1b shows the bract structure of pure $ZnIn_2S_4$ composed of many lamellar petals. Figs. 1c-e show SEM images of MoS_2, Ni-Mo-S (Ni:Mo = 1:2) and Ni-Mo-S (Ni:Mo =1:1) respectively. It can be seen that their aggregates are

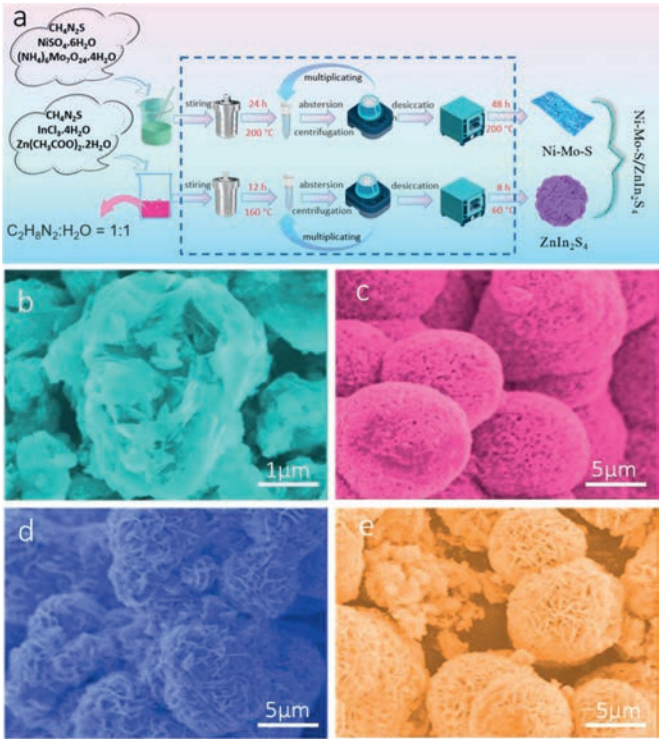

Fig. 1. (a) Schematic illustration of the synthesis of Ni doped $MoS_2/ZnIn_2S_4$ composite. SEM images of (b) $ZnIn_2S_4$, (c) MoS_2, (d) Ni-Mo-S (Ni:Mo = 1:2), (e) Ni-Mo-S (Ni:Mo = 1:1).

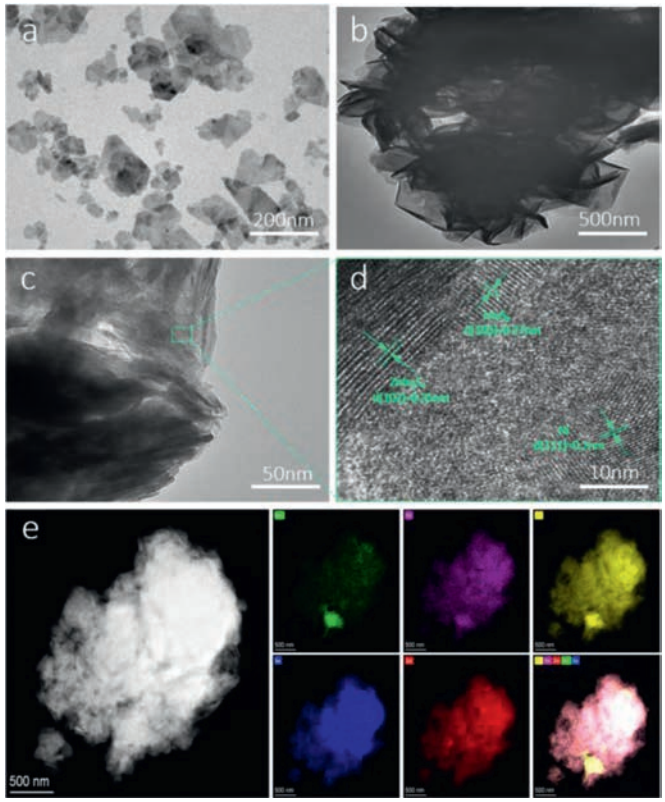

Fig. 2. TEM images of (a) $ZnIn_2S_4$ and (b) Ni-Mo-S (Ni:Mo = 1:2). (c) TEM and (d) high resolution TEM images of Ni-Mo-S/$ZnIn_2S_4$ (Ni:Mo = 1:2) composites. (e) The corresponding EDX mapping images of Mo, Ni, S, In and Zn of Ni-Mo-S/$ZnIn_2S_4$ (Ni:Mo = 1:2) composites.

similar in morphology. The diameter of microspheres is about 1.0 μm to 4.0 μm, and the edges are serrated, indicating that the microspheres are made up of a large number of interlaced flakes. This also shows that the doping of Ni^{2+} with different mole ratio hardly changes the morphology of MoS_2. Due to the similar layered structure of $ZnIn_2S_4$ and Ni-Mo-S, the Ni-Mo-S nanosheets can be closely loaded on the $ZnIn_2S_4$ nanoflowers for self-assembly to form heterojunctions.

The detailed microstructure of $ZnIn_2S_4$, Ni-Mo-S and Ni-Mo-S/$ZnIn_2S_4$ samples were studied by TEM and HRTEM. The TEM in Fig. 2a shows that $ZnIn_2S_4$ has a lamellar structure with relatively transparent characteristics, indicating that $ZnIn_2S_4$ nanoscale flowers have ultrathin properties. In Fig. 2b, the gauze mesh edges of the nanoflower can be clearly observed to further verify that the synthesized Ni-Mo-S was formed by stacking and self-assembling thin nanosheets. This is consistent with the SEM image in Fig. 1d. It is also found that the edge of Ni-Mo-S nanosheets is curly. This phenomenon may be attributed to the instability of the ultra-thin nanosheet, which forms a closed structure by rolling up to eliminate dangling bonds at the edges and minimizing its surface energy. As can be seen from the TEM pattern of Ni-Mo-S/$ZnIn_2S_4$ composite in Fig. 2c, the accumulation of Ni-Mo-S/$ZnIn_2S_4$ nanosheets is relatively loose, which may be due to the mutual blocking of the formation and stacking of Ni-Mo-S and $ZnIn_2S_4$ nanosheets during the synthesis process. The intersecting lattice fringes in the HRTEM image (Fig. 2d) confirm the close contact between the Ni-Mo-S nanosheets and the $ZnIn_2S_4$ nanoflowers. The lattice spacing of 0.35 nm corresponds to plane (102) of $ZnIn_2S_4$. The lattice spacing of 0.27 nm and 0.2 nm matched well with the (100) plane of MoS_2 and (111) plane of Ni, respectively, indicating that Ni is successfully doped into MoS_2 to form Ni-Mo-S. The map of EDX elements in Fig. 2e shows that Mo, Ni, S, In and Zn are uniformly distributed in the whole Ni-Mo-S/$ZnIn_2S_4$ composite. Therefore, it is reasonable to believe that two-dimensional Ni-Mo-S/$ZnIn_2S_4$ heterostructures with close interfacial contact have been constructed.

The composition and chemical states of the prepared Ni-Mo-S/$ZnIn_2S_4$ composites were measured and analyzed by X-ray photoelectron spectroscopy (XPS). According to the full spectrum shown in Fig. 3a, the prepared catalyst is composed of S, In, Zn, Mo and Ni elements. Figs. 3b-f show the high-resolution XPS spectra of different elements in the Ni-Mo-S/$ZnIn_2S_4$ composite. In the XPS signal of composite In 3d (Fig. 3b), the peaks of 444.8 eV and 452.4 eV are attributed to In $3d_{5/2}$ and In $3d_{3/2}$, respectively, indicating the presence of In^{3+} [43]. The peaks at 1021.5 eV and 1044.6 eV observed in Fig. 3c correspond to Zn $2p_{3/2}$ and Zn $2p_{1/2}$ respectively, indicating that Zn is in +2 oxidation state [44]. In the spectrum of Ni 2p (Fig. 3d), the binding energy is located in two strong peaks of 857.1 eV and 870 eV, which are derived from the Ni $2p_{3/2}$ and Ni $2p_{1/2}$ corresponding to the Ni^{2+} and Ni-S bonds in Ni-Mo-S, respectively [45]. The XPS spectrum of S 2p can be convolved into two peaks (Fig. 3e) with the binding energy located at 161.6 eV and 163.3 eV, which are respectively assigned to S $2p_{1/2}$ and S $2p_{3/2}$, corresponding to the −2 reduction state of S [46]. In Fig. 3f, the peaks with binding energies of 228.2 eV and 232.3 eV are allocated to Mo $3d_{5/2}$ and Mo $3d_{3/2}$, respectively, confirming +4 oxidation state of Mo [47]. In addition, the peak value at 225.6 eV corresponds to the transition of S 2s [18]. The above XPS results confirm the presence of S, In, Zn, Mo and Ni elements, which is consistent with the chemical composition of Ni-Mo-S/$ZnIn_2S_4$.

The optical absorption characteristics of $ZnIn_2S_4$/Ni-Mo-S (Ni:Mo = 1:2) composites were measured by UV-visible diffuse reflectance spectroscopy (DRS) (Fig. 3g). The absorption band of pure $ZnIn_2S_4$ ends in the visible light region around 540 nm, showing a weak light absorption characteristic. $ZnIn_2S_4$/Ni-Mo-S nanocom-

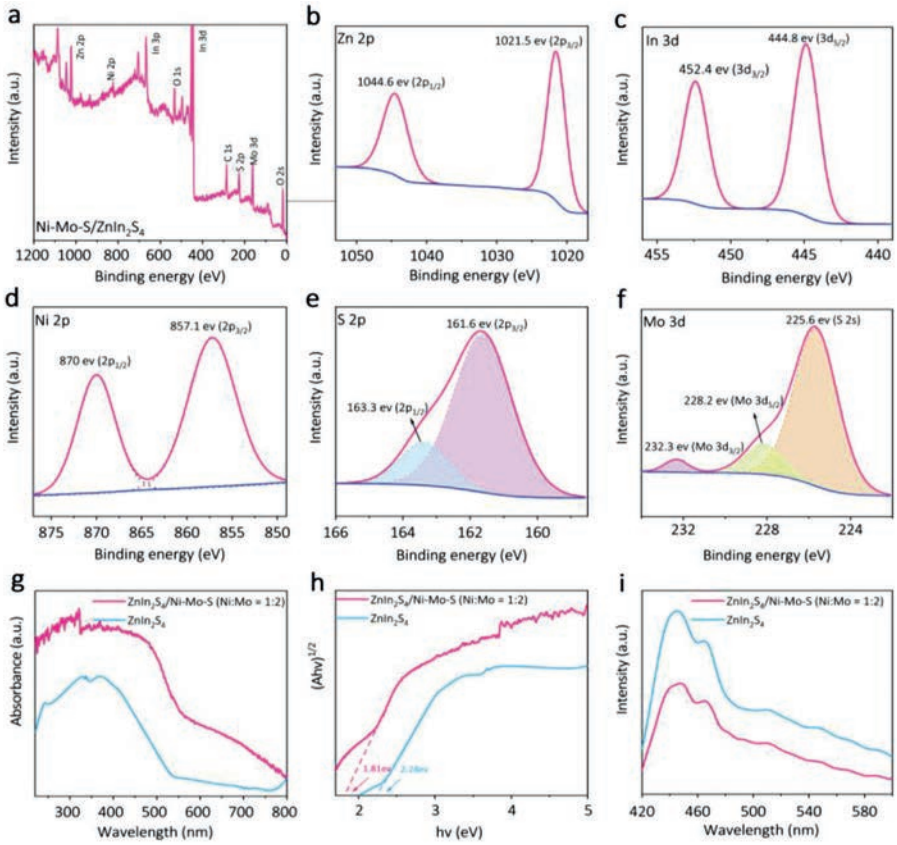

Fig. 3. (a) Survey spectra of $ZnIn_2S_4$/Ni-Mo-S (Ni:Mo = 1:2) composites photocatalyst. High resolution XPS imagesof (b) Zn 2p, (c) In 3d, (d) Ni 2p, (e) S 2p, (f) Mo 3d. (g) UV–vis DRS spectra, (h) Tauc plots, (i) photoluminescence (PL) spectra of $ZnIn_2S_4$ and $ZnIn_2S_4$/Ni-Mo-S (Ni:Mo = 1:2).

posites show a wider range of light absorption and stronger absorption intensity. $ZnIn_2S_4$/Ni-Mo-S has a characteristic absorption corresponding to $ZnIn_2S_4$ in the region of 500–700 nm, and the enhanced absorption is related to the absorption of Ni-Mo-S. Tauc plots of $ZnIn_2S_4$ and $ZnIn_2S_4$/Ni-Mo-S were plotted based on the results of UV-vis DRS, as shown in Fig. 3h. In general, the semiconductor band gap energy (E_g) is estimated by the following equation: $(\alpha h\nu)^{1/n} = A\ (h\nu - E_g)$. The band gap energies of $ZnIn_2S_4$, $ZnIn_2S_4$/Ni-Mo-S are calculated to be 2.24 eV and 1.81 eV, respectively. The narrower band gap of $ZnIn_2S_4$/Ni-Mo-S composites is conducive to charge separation. This shows the advantages of $ZnIn_2S_4$/Ni-Mo-S composite materials, which can make $ZnIn_2S_4$ more effective use of visible light and enhance the photocatalytic performance. In order to study charge migration in the composite photocatalyst, we measured the photoluminescence (PL) spectra of pure $ZnIn_2S_4$ and $ZnIn_2S_4$/Ni-Mo-S composites, as shown in Fig. 3i. It is well known that the stronger the intensity of PL peak is, the greater the probability of recombination of electron holes in the corresponding photocatalyst [48]. The PL peak of $ZnIn_2S_4$/Ni-Mo-S composite is significantly lower than that of pure $ZnIn_2S_4$, which proves that $ZnIn_2S_4$/Ni-Mo-S can effectively inhibit the recombination of electron hole pairs, which is helpful to the separation of electron holes and improve photocatalytic performance.

Emerging experimental results and theoretical predictions suggest that MoS_2 is a promising alternative to inexpensive, earth-abundant and visible responsive catalysts [49,50]. However, catalytic activity is limited by the low active site exposure and the high kinetic energy barrier of water decomposition in EY/TEOA and Na_2S/Na_2SO_3 system. Accordingly, the photocatalytic hydrogen evolution performance of Ni-doped MoS_2 as cocatalyst in lactic acid, EY/TEOA and Na_2S/Na_2SO_3 systems were evaluated by photocatalytic hydrogen generation.

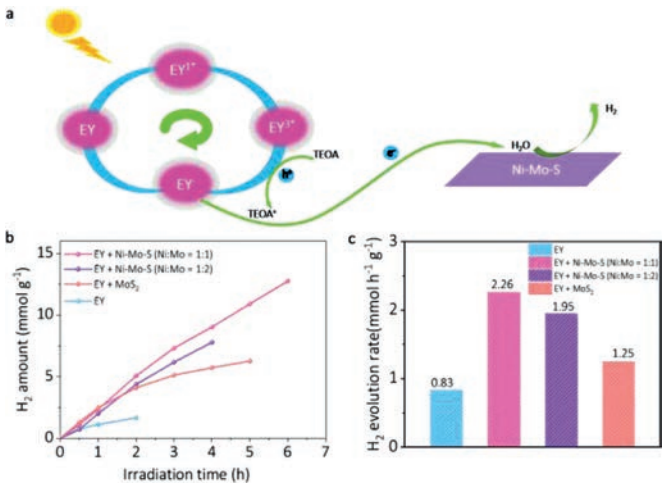

Fig. 4. (a) Diagram of carrier migration process of Ni-Mo-S in EY/TEOA aqueous solution (pH 7) under visible light irradiation. (b, c) Comparison of photocatalytic H_2 evolution activities over EY, MoS_2/EY, Ni-Mo-S/EY (Ni:Mo = 1:2) and Ni-Mo-S/EY (Ni:Mo = 1:1)

In the EY/TEOA system, we discussed the formation mechanism of hydrogen generation using EY as sensitizer, TEOA hole scavenger and Ni-Mo-S nanosheet as catalyst. Fig. 4a shows the schematic diagram of the electron transfer process of EY/Ni-Mo-S under visible light irradiation. The reaction is triggered by the light excitation of EY to produce the triple excited state (EY^{3*}). Then, through reduction quenching, electrons are extracted from TEOA to produce free radical EY^-. Electrons are easily transferred from highly reductive EY^- to Ni-Mo-S nanosheets to reduce H^+ generated by H_2O

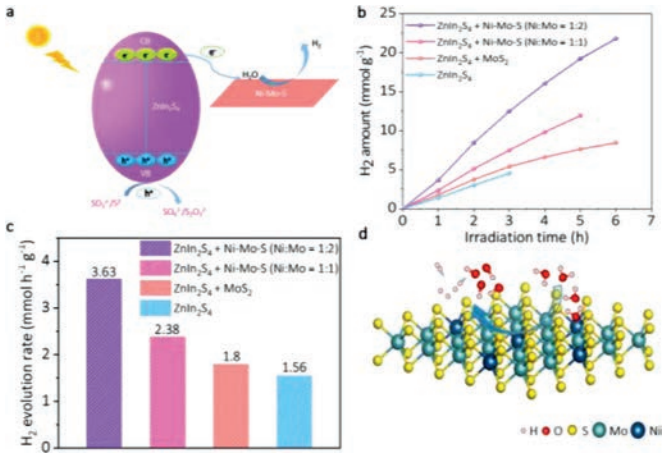

Fig. 5. (a) Schematic of the charge carrier migration process of Ni-Mo-S/$ZnIn_2S_4$ composites in Na_2S/Na_2SO_3aqueous solution (pH 13.2) under visible light irradiation. (b, c) Comparison of photocatalytic H_2 evolution activities over $ZnIn_2S_4$, $MoS_2/ZnIn_2S_4$, Ni-Mo-S/$ZnIn_2S_4$ (Ni:Mo = 1:2) and Ni-Mo-S/$ZnIn_2S_4$ (Ni:Mo = 1:1). (d) Atomic structure diagram of Ni-Mo-S nanosheets for H_2O dissociation.

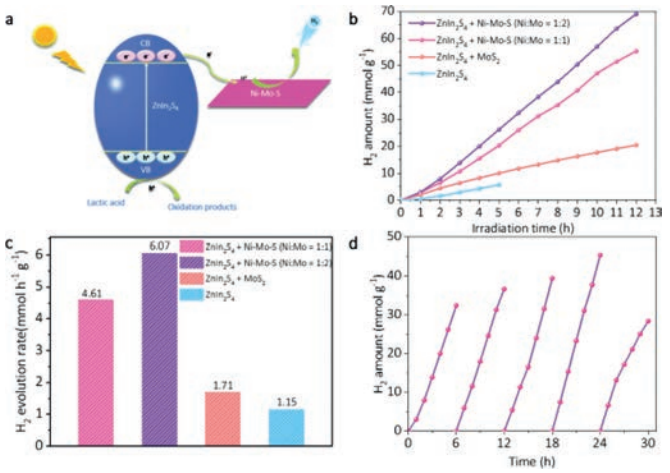

Fig. 6. (a) Schematic of the charge carrier migration process of Ni-Mo-S/$ZnIn_2S_4$ composites in lactic acid aqueous solution (pH 2.5) under visible light irradiation. (b, c) Comparison of photocatalytic H_2 evolution activities over $ZnIn_2S_4$, $MoS_2/ZnIn_2S_4$, Ni-Mo-S/$ZnIn_2S_4$ (Ni:Mo = 1:2) and Ni-Mo-S/$ZnIn_2S_4$ (Ni:Mo = 1:1). (d) Cycling test of catalytic H_2 generation from Lactic acid solution over the Ni-Mo-S/$ZnIn_2S_4$ (Ni:Mo = 1:2) nanocomposite.

decomposition to form an excited state H*. Two excited states H* react with each other to produce H_2. In Fig. 4b, the hourly H_2 dynamic productivity of different photocatalytic materials in the process of HER was tracked by a constant online detection system. It can be seen that the hydrogen evolution performance was significantly improved after the addition of cocatalyst in EY. With the increase of the ratio of Ni:Mo in Ni-Mo-S, the amount of hydrogen evolution increased. When the value of Ni:Mo is equal to 1:1, the catalytic performance is the best, and the maximum H_2 production rate reaches 2.26 mmol h^{-1} g^{-1} (Fig. 4c). Therefore, Ni doped MoS_2 nanosheets (Ni-Mo-S) can promote photocatalytic hydrogen evolution in EY/TEOA aqueous solution.

In the Na_2S/Na_2SO_3 system, the slow HER kinetics of MoS_2 catalyst is improved by the design of hydrolysis dislocation by doping Ni atoms into MoS_2 nanosheets. The introduced Ni site can not only effectively reduce the energy barrier of initial water dissociation, but also promote the desorption of OH^- [33,51]. Fig. 5a shows the Ni-Mo-S/$ZnIn_2S_4$ composite under visible light irradiation, with Na_2S/Na_2SO_3 as the hole sacrifice agent, and the photogenerated electrons are excited from valence band (VB) of $ZnIn_2S_4$ to conduction band (CB). Since the CB of $ZnIn_2S_4$ is more negative than that of Ni-Mo-S, the photogenerated electrons on $ZnIn_2S_4$ CB can be quickly transferred to Ni-Mo-S, which promotes the separation of photogenerated electron-hole pairs and inhibits the recombination. Under the action of electrons, the H^+ of H_2O decomposition is reduced to the excited state H*, and the two excited states H* combine to produce H_2. Fig. 5b shows the H_2 dynamic productivity per hour of different photocatalytic materials in the HER process. It can be found that when the Ni:Mo value of co-catalyst Ni-Mo-S nanosheets is 1:2, the hydrogen evolution performance is the best, and the maximum H_2 production rate can reach 3.63 mmol h^{-1} g^{-1} (Fig. 5c). In Fig. 5d, the doping of Ni in MoS_2 not only activates the S atoms around it, but also accelerates the dissociation of water and promotes the desorption of the formed OH^-, which greatly improves the activity of hydrogen production. Therefore, Ni-Mo-S as co-catalyst in Na_2S/Na_2SO_3aqueous solution can also improve the efficiency of hydrogen production.

Then we studied the photocatalytic hydrogen evolution performance of Ni-Mo-S nanosheets as co-catalyst in lactic acid system. Fig. 6a shows Ni-Mo-S/$ZnIn_2S_4$ composite material under visible light irradiation with lactic acid as sacrificial agent. Photogenerated electrons excited by $ZnIn_2S_4$ are transferred to Ni-Mo-S nanosheets. Under the action of electrons, H^+ in solution is reduced to the excited state H*, which then combines with H^+ in solution to produce H_2. Fig. 6b shows the kinetic process of H_2 production by different samples at HER per hour. Pure $ZnIn_2S_4$ photocatalyst shows poor photocatalytic H_2 production activity with a hydrogen production rate of 1.15 mmol h^{-1} g^{-1} (Fig. 6c). Compared with Fig. 5, the hydrogen production rate of pure $ZnIn_2S_4$ in the Na_2S/Na_2SO_3 system is higher (1.56 mmol h^{-1} g^{-1}), indicating that Na_2S/Na_2SO_3 is more suitable for the electron donor in the $ZnIn_2S_4$ system. When $ZnIn_2S_4$ is combined with MoS_2 nanosheet, it can be observed that the H_2 yield is increased compared with that of pure $ZnIn_2S_4$, because MoS_2 acts as a cocatalyst to accelerate the separation of electron-hole pairs. However, due to the existence of MoS_2 inert substrate surface, the hydrogen evolution performance is still limited. The ability of H_2 generation is significantly improved when the Ni doped MoS_2 nanosheets (Ni-Mo-S) were coupled with $ZnIn_2S_4$ to form heterogeneous composite photocatalyst. When the Ni:Mo value of co-catalyst Ni-Mo-S nanosheets is 1:2, the hydrogen evolution performance is the best. The maximum hydrogen production rate of H_2 can reach 6.07 mmol h^{-1} g^{-1}, which is 5.28 times that of pure $ZnIn_2S_4$.

Therefore, the Ni-Mo-S co-catalyst in lactic acid system can greatly enhance the efficiency of hydrogen production. Table S1 (Supporting information) provides the photocatalytic hydrogen evolution activity of some recently studied $ZnIn_2S_4$-based photocatalysts.

It is well known that the stability of catalysts plays an important role in practical applications. The hydrogen evolution reaction of the optimized Ni-Mo-S/$ZnIn_2S_4$ (Ni:Mo = 1:2) photocatalyst is carried out to evaluate its photocatalytic stability. As shown in Fig. 6d, 5 cycles were tested, each cycle being 6 h. In the first 4 cycles, the hydrogen production rate of each cycle is gradually improved, and the hydrogen production performance is getting better and better. The reduced activity of the photocatalyst in the fifth cycle may be due to the consumption of sacrificial agents. However, after the fifth cycle, the hydrogen production efficiency is still about 88% of the initial efficiency, and the surface Ni-Mo-S/$ZnIn_2S_4$ photocatalyst still retains its original activity to a large extent after 30 h reaction. Therefore, the prepared Ni-Mo-S/$ZnIn_2S_4$ (Ni:Mo = 1:2) as a photocatalyst in acidic medium has high stability and good recovery, which is conducive to large-scale production and application.

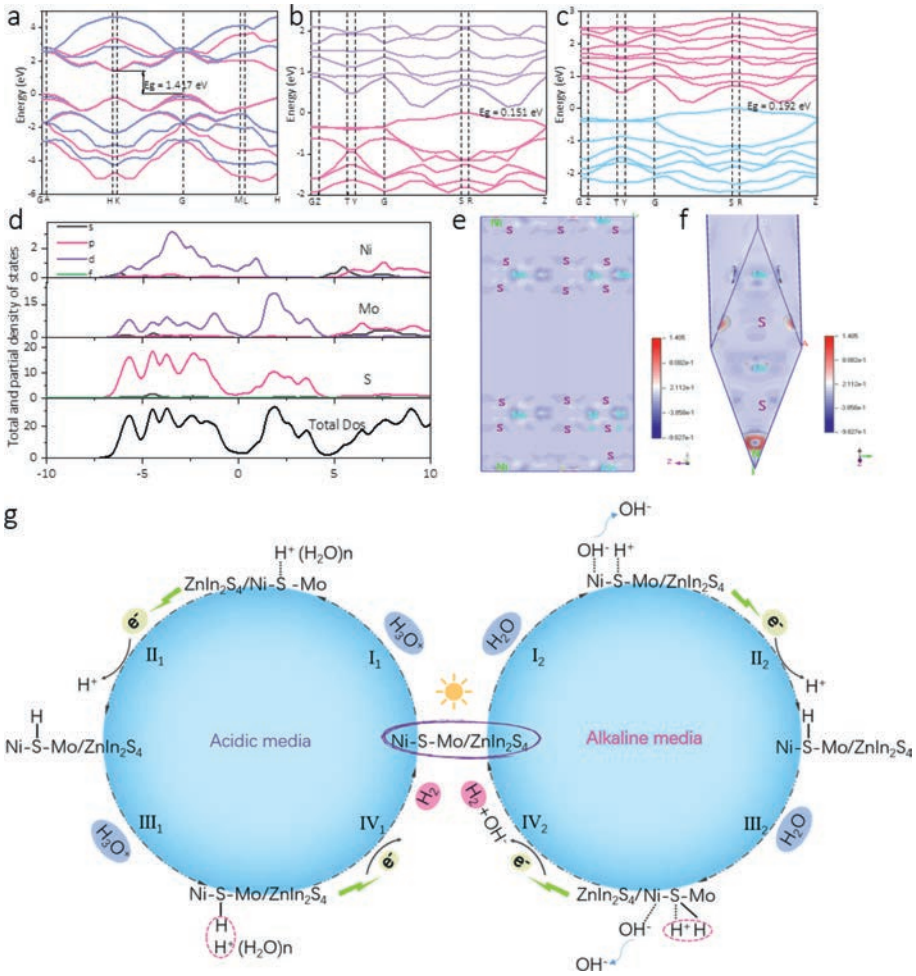

Fig. 7. The band structure of (a) pure MoS_2, (b) Ni replaces the edge Mo position of MoS_2. (c) Ni replaces the middle Mo position of MoS_2. (d) The partial and total density of states. (e, f) The charge density difference of MoS_2 where the edge Mo is replaced by Ni. (g) Correlation of HER mechanism in lactic acid and Na_2S/Na_2SO_3 system. Left: HER mechanism of Ni-Mo-S/$ZnIn_2S_4$ in lactic acid aqueous solution; Right: HER mechanism of Ni-Mo-S/$ZnIn_2S_4$ in Na_2S/Na_2SO_3 aqueous solution.

Therefore, through the above three diverse systems, we experimentally confirm that the introduction of Ni site in MoS_2 greatly enhance HER activity.

In order to analyze the electronic structure of Ni-Mo-S, the energy band structure, density of states and charge density difference are calculated. In Figs. 7a-c, the band gaps of the pure MoS_2 and Ni substituting for the edge Mo sites of MoS_2 and the middle Mo sites of MoS_2 are calculated respectively. Fig. S1 (Supporting information) further shows its atomic structure. The figure shows that the band gap significantly decreases after the introduction of Ni, from 1.471 eV of pure MoS_2 to 0.151 eV of minimum band gap. The Significant reduction of the band gap is conducive to rapid charge transfer and improved HER efficiency.

The partial and total density of states of Mo sites at the edge of Ni substituted MoS_2 are calculated in Fig. 7d. It can be clearly seen that the atomic contribution of Ni 3d is the main contribution to the top of the valence band and the bottom of the conduction band of Ni-Mo-S. The charge density difference shows the charge transfer between atoms. In order to understand the electron transfer process in Ni-Mo-S, the charge density difference is calculated, as shown in Figs. 7e and f. The results show that more electrons are obtained on the Ni site than on the Mo site. It is theoretically proved that the performance of HER can be greatly improved by introducing Ni into MoS_2.

Fig. 7g illustrates the optimized HER mechanism of Ni-Mo-S/$ZnIn_2S_4$ in lactic acid and Na_2S/Na_2SO_3 system. Under visible light irradiation, the hydrated ions and water are preferentially adsorbed to the Ni-doped activated S sites (step I_1 and step I_2). In lactic acid aqueous solution, the adsorbed H_3O^+ is reduced on the surface by an electron excited from $ZnIn_2S_4$ to form the adsorbed H atom (Step II_1). Finally, another proton from the adjacent H_3O^+ reacts with the first adsorbed H atom to produce H_2 (Step III_1-IV_1). In Na_2S/Na_2SO_3aqueous solution, the mechanism of overcoming the kinetic barrier of hydrolysis dissociation has been found. We believe that water splitting occurs at the Ni site, leading to the fracture of the HO-H bond, forming adsorbed OH^- and H^+, which are adsorbed at the Ni and S sites, respectively. However, the adsorbed OH^- at the Ni site can easily break free and return to the medium, while the adsorbed H^+ at the S site is reduced by an electron to form the adsorbed H atom (Step II_2). The last two adsorbed H atoms react to form H_2 (Step III_2-IV_2). Therefore, it is theoretically confirmed that HER dynamics can be greatly improved by introducing Ni sites.

In conclusion, we have shown that the catalytic activity of Ni-Mo-S can be greatly improved in the multi-reaction systems, whether as catalyst or co-catalyst. Firstly, we prepared Ni-Mo-S nanosheets by a simple hydrothermal method. It can be found by TEM that Ni is successfully doped into MoS_2. Secondly, in the experiment, the experimental data of the multi-reaction systems proved that Ni-Mo-S as a catalyst has significantly enhanced catalytic hydrogen evolution performance and excellent catalytic stability. Finally, our theoretical calculations show that the doping of

Ni plays a crucial role in the Ni-Mo-S nanostructure. Ni-Mo-S has a narrower band gap, and the Ni in Ni-Mo-S has the main atomic contribution at the top of valence band and the bottom of conduction band, and has more electrons at the Ni site. The above experiments and theories have confirmed the key role of Ni doped MoS_2 in improving its catalytic performance. These findings in the current work provide some new clues for the development of large-scale production, multi-reaction systems and inexpensive photocatalyst.

Declaration of competing interest

We declare that we have no financial and personal relationships with other people or organizations that can inappropriately influence our work, there is no professional or other personal interest of any nature or kind in any product, service and/or company that could be construed as influencing the position presented in, or the review of, the manuscript entitled.

Acknowledgments

The authors acknowledge financial support from the National Natural Science Foundation of China (Nos. 11974188,11304159), the China Postdoctoral Science Foundation (Nos. 2021T140339, 2018M632345), the Qing Lan Project of Jiangsu Province, the Natural Science Foundation of Jiangsu Province (Nos. BK20201381, BK20161512), and NUPTSF (No. NY218022).

Supplementary materials

Supplementary material associated with this article can be found, in the online version, at doi:10.1016/j.cclet.2021.08.103.

References

[1] L. Lin, P. Sherrell, Y. Liu, et al., Adv. Energy Mater. 10 (2020) 1903870.
[2] L. Xie, L. Wang, W. Zhao, et al., Nat. Commun. 12 (2021) 5070.
[3] H. Yang, C. He, L. Fu, et al., Chin. Chem. Lett. 32 (2021) 3202–3206.
[4] Y. Liu, H. Wang, X. Yuan, et al., Chem. Catal. 1 (2021) 44–68.
[5] S. Zhang, X. Liu, C. Liu, et al., ACS Nano 12 (2018) 751–758.
[6] S. Zhang, L. Wang, C. Liu, et al., Water Res. 121 (2017) 11–19.
[7] L. Fu, R. Wang, C. Zhao, et al., Chem. Engin. J. 414 (2021) 128857.
[8] N. Zhao, L. Wang, Z. Zhang, et al., ACS Appl. Mater. Interfaces 11 (2019) 42014–42020.
[9] Y. Zhou, J. Zhang, E. Song, et al., Nat. Commun. 11 (2020) 2253.
[10] R. Wang, C. He, W. Chen, et al., Chin. Chem. Lett. (2021) doi.org/10.1016/j.cclet.2021.05.024.
[11] L. Wang, L. Xie, W. Zhao, S. Liu, Q. Zhao, Chem. Eng. J. 405 (2021) 127028.
[12] Y. Zhu, L. Wang, Y. Liu, et al., Appl. Catal. B 241 (2019) 483–490.
[13] L. Jiang, K. Wang, X. Wu, et al., ACS Appl. Mater. Interfaces 11 (2019) 26898–26908.
[14] G. Swain, S. Sultana, K. Parida, et al., ACS Sustainable Chem. Eng. 8 (2020) 4848–4862.
[15] J. Cavin, A. Ahmadiparidari, L. Majidi, et al., Adv. Mater. 33 (2021) 2100347.
[16] X. Cai, Z. Zeng, Y. Liu, et al., Appl. Catal. B 297 (2021) 120391.
[17] M.Q. Yang, Y.J. Xu, W. Lu, et al., Nat. Commun. 8 (2017) 14224.
[18] Y.J. Yuan, J.R. Tu, Z.J. Ye, et al., Appl. Catal. B 188 (2016) 13–22.
[19] E. Zhang, Q. Zhu, J. Huang, et al., Appl. Catal. B 293 (2021) 120213.
[20] Y. Zhu, J. Chen, L. Shao, et al., Appl. Catal. B 268 (2020) 118744.
[21] T.H.M. Lau, X. Lu, J. Kulhavy, et al., Chem. Sci. 9 (2018) 4769–4776.
[22] K. Sun, L. Zeng, S. Liu, et al., Nano Energy 58 (2019) 862–869.
[23] Q. Wang, Z.L. Zhao, S. Dong, et al., Nano Energy 53 (2018) 458–467.
[24] W. Wu, C. Niu, C. Wei, et al., Angew. Chem. Int. Ed. 58 (2019) 2029–2033.
[25] L. Yin, X. Hai, K. Chang, et al., Small 14 (2018) e1704153.
[26] Y. Zang, S. Niu, Y. Wu, et al., Nat. Commun. 10 (2019) 1217.
[27] H. Duan, C. Wang, G. Li, et al., Angew. Chem. Int. Ed. 60 (2021) 7251–7258.
[28] X. Huang, M. Leng, W. Xiao, et al., Adv. Funct. Mater. 27 (2017) 1604943.
[29] H. Li, C. Tsai, A.L. Koh, et al., Nat. Mater. 15 (2016) 48–53.
[30] Y. Li, L. Wang, S. Zhang, et al., Catal. Sci. Technol. 7 (2017) 718–724.
[31] L. Loh, Z. Zhang, M. Bosman, et al., Nano Res. 14 (2020) 1668–1681.
[32] K. Qi, X. Cui, L. Gu, et al., Nat. Commun. 10 (2019) 5231.
[33] J. Zhang, T. Wang, P. Liu, et al., Energy Environ. Sci. 9 (2016) 2789–2793.
[34] L. Xu, J. Zeng, Q. Li, et al., Appl. Surf. Sci. 547 (2021) 149207.
[35] Y. Chen, S. Ji, W. Sun, et al., Angew. Chem. Int. Ed. 59 (2020) 1295–1301.
[36] Y. Lei, Y. Wang, Y. Liu, et al., Angew. Chem. Int. Ed. 59 (2020) 20794–20812.
[37] L.S. Zhang, X.H. Jiang, Z.A. Zhong, et al., Angew. Chem. Int. Ed. 32 (2021) 21751–21755.
[38] X.H. Jiang, F. Yu, D.S. Wu, et al., Chin. Chem. Lett. 32 (2021) 2782–2786.
[39] X.H. Jiang, L.S. Zhang, H.Y. Liu, et al., Angew. Chem. Int. Ed. 59 (2020) 23112–23116.
[40] M. Zhu, L.S. Zhang, S.S. Liu, et al., Chin. Chem. Lett. 31 (2020) 1961–1965.
[41] F. Yu, L.C. Wang, Q.J. Xing, et al., Chin. Chem. Lett. 31 (2020) 1648–1653.
[42] J.P. Zou, Y. Chen, S.S. Liu, et al., Water Res. 150 (2019) 330–339.
[43] W. Li, Z. Lin, G. Yang, et al., Nanoscale 9 (2017) 18290–18298.
[44] G. Swain, S. Sultana, K. Parida, et al., Inorg. Chem. 58 (2019) 9941–9955.
[45] X. Shi, L. Mao, C. Dai, et al., J. Mater. Chem. A 8 (2020) 13376–13384.
[46] C. Sun, M. Liu, L. Wang, et al., Chin. Chem. Lett. (2021) doi.org/10.1016/j.cclet.2021.08.052.
[47] Y.J. Yuan, D. Chen, J. Zhong, et al., J. Mater. Chem. A 5 (2017) 15771–15779.
[48] Y. Li, L. Wang, T. Cai, et al., Chem. Eng. J. 321 (2017) 366–374.
[49] Z. Luo, H. Zhang, Y. Yang, et al., Nat. Commun. 11 (2020) 1116.
[50] J. Deng, H. Li, S. Wang, et al., Nat. Commun. 8 (2017) 14430.
[51] J.J.L. Humphrey, R. Kronberg, R. Cai, et al., Nanoscale 12 (2020) 4459–4472.